Journal of Photochemistry & Photobiology, A: Chemistry 436 (2023) 114349

Contents lists available at ScienceDirect

Journal of Photochemistry & Photobiology, A: Chemistry

journal homepage: www.elsevier.com/locate/jphotochem

# Hyaluronic acid-poly(lactic-co-glycolic acid) nanoparticles with a ruthenium photosensitizer cargo for photokilling of oral cancer cells

José Quílez-Alburquerque [a,b], Mohammad Ahsan Saad [b], Ana B. Descalzo [a], Guillermo Orellana [a,*], Tayyaba Hasan [b,c,*]

[a] Department of Organic Chemistry, Faculty of Chemistry, Complutense University of Madrid, 28040 Madrid, Spain
[b] Wellman Center for Photomedicine, Massachusetts General Hospital and Harvard Medical School, 40 Blossom St, Boston, MA 02114, USA
[c] Division of Health Sciences and Technology, Harvard University and Massachusetts Institute of Technology, Cambridge, MA 02139, USA

ARTICLE INFO

*Keywords:*
Photodynamic therapy
Ru(II) complex
Hyaluronic acid-poly(lactic-*co*-glycolic acid)
Superoxide anion

ABSTRACT

Photodynamic therapy (PDT), a combination of light, molecular oxygen and a photosensitizing dye, has gained attention as a promising technique to treat various types of cancers. Among all the photosensitizers reported so far, ruthenium(II) polypyridyl complexes exhibit unique photophysical and photobiological features owing to their photostability, μs triplet excited states, and ability to undergo both 'type I' and 'type II' reactions in their photodynamic action. We report the synthesis of a novel Ru(II) complex containing one 2,2′-biimidazole (bim) and two tetramethylphenanthroline (tmp) ligands that sensitizes the simultaneous production of superoxide anion ($O_2^{\bullet-}$) and singlet oxygen ($^1O_2$) upon irradiation with blue-green light. To improve its solubility and bioavailability, a zero-order degradation-controlled release formulation based on self-assembled hyaluronic acid (HA)–poly(lactic-*co*-glycolic acid) (PLGA) nanoparticles (NPs) was prepared for its topical application in oral cancer cells (TR146 cell line). These NPs (152 nm diameter) showed 70 % Ru-complex encapsulation efficiency, high physiological stability, low polydispersity index (0.12), and a sensitizer release enhanced by the hyaluronidase enzyme overexpressed in many cancer cells. Both the free complex and its nanocarrier are internalized by the TR146 cells, displaying > 90 % in vitro cytotoxicity under 470 nm activation (50 J $cm^{-2}$), highlighting their potential as PDT agents. The Ru(II) complex loaded nanocarrier developed in this study can be potentially effective in the treatment of oral cancers.

## 1. Introduction

Oral cancer represents 3 % of the annually diagnosed cancer cases in United States. However, this rate is much higher in countries such as India, where this oral disease accounts for more than 30 % of the cancer cases. The standard treatment is surgery followed by radiotherapy or chemotherapy with 5-year survival rates below 60 % [1]. For this reason, alternative treatments are highly needed. Photodynamic therapy (PDT) has emerged as an alternative for the treatment of different cancerous and non-cancerous malignancies [2–5]. PDT relies on the ability of a dye ('photosensitizer') to generate cytotoxic reactive oxygen species (ROS) upon light-activation at an absorption wavelength specific for the photosensitizer in the presence of molecular oxygen ($^3O_2$). If the dye is bound to the cell membrane or internalized, the ROS generation leads to significant cellular damage and, eventually, cell death. In most cases, upon collision, the triplet excited state of the photosensitizer transfers its energy to $^3O_2$ molecules yielding the highly reactive and short-lived singlet oxygen species ($^1O_2$), through the so-called 'Type II' mechanism [6]. On the other hand, 'Type I' mechanism involves an electron transfer from the surrounding biomolecules to the photoexcited photosensitizer with subsequent formation of superoxide anion ($O_2^{\bullet-}$) and other ROS from $O_2$ [6]. In the presence of intracellular superoxide dismutase (SOD), $O_2^{\bullet-}$ can be transformed into hydrogen peroxide ($H_2O_2$) and more $^3O_2$ that could be recycled during this cascade reaction [6–9]. The accumulated $H_2O_2$ could be further transformed into the highly toxic hydroxyl radical (HO•) that aggravates oxidative damage enhancing PDT [6,10].

Among all the investigated photosensitizers, transition metal complexes offer advantages as potential PDT agents [11]. Several laboratories are engaged in exciting research related to the preclinical and clinical evaluation of such complexes [12,13]. In particular, luminescent Ru(II) polypyridyl complexes exhibit unique photophysical and

* Corresponding authors.
*E-mail addresses:* orellana@quim.ucm.es (G. Orellana), thasan@mgh.harvard.edu (T. Hasan).

https://doi.org/10.1016/j.jphotochem.2022.114349
Received 10 May 2022; Received in revised form 7 October 2022; Accepted 13 October 2022
Available online 20 October 2022

photochemical features owing to their low toxicity in the dark, thermal inertia and photostability, μs-lived triplet excited states, near diffusion-controlled triplet quenching rate constants with $^3O_2$, and their ability to undergo Type I and Type II reactions for their photodynamic action [14,15]. Moreover, their photoactivated properties can be tuned by a judicious selection of their metal-chelating ligands. Noteworthy, the α-terthienyl imidazophenanthroline Ru(II) complex TLD1433 prepared by McFarland's group [12] has entered phase II clinical trials in Canada for Type I/Type II PDT of non-muscle invasive bladder cancer, underlining the potential usefulness of these transition metal complexes. Due to the lack of absorption in the NIR-PDT window, these Ru(II) complexes could be applied topically in the treatment of early-stage oral cancers and disinfection of wounds where deep tissue irradiation is not a prerequisite [16,17].

However, the poor selectivity for cancerous tissues limits the clinical application and poses challenges for using Ru(II) photosensitizers. To overcome this limitation, the quest for specific metal-chelating ligands is a necessity. In this context, imidazole derivatives have been identified as biologically active compounds in multiple applications [18]. Their antimycobacterial, antifungal and anticancer activity, both in vivo and in vitro, have been demonstrated [19–21]. Furthermore, their imino moiety can coordinate the Ru(II) ion. Several Ru(II)-imidazolate complexes, such as NAMI-A or NKP-1339, have progressed to different stages in clinical trials as potential anticancer agents and alternatives to cisplatin [22,23]. Notably, some studies have reported the use of 2,2′-biimidazole (bim) coordination complexes as possible antitumor agents [24]. Metal-bim complexes display anion-recognition features (sensing of acetates and diketonates has been demonstrated with luminescent Ru(II)-bim complexes) [25], anion transport through lipophilic membranes (luminescent Ir(III)-bim complexes) [26], lysosomal pH monitoring and DNA sensors (fluorometric and colorimetric Ru(II)-bim sensors, respectively) [27], G-quadruplex DNA-recognizing Ru(II)-bim complexes [28], and sensitizers for mitochondria-targeted PDT (cyclometalated Ir(III)-bim complexes) [29]. Moreover, the π-excessive character of the 2,2′-biimidazole ligand results in a more negative $Ru^{3+/2+*}$ redox potential [30], which favors direct electron transfer from the photoexcited Ru(II)-bim complexes to $^3O_2$ generating $O_2^{\bullet-}$, a variation of the type I PDT mechanism [31].

In this regard, we have designed and prepared a novel heteroleptic Ru(II)-bim complex (Figs. S1-S2, Supporting Information), with potentially enhanced photodynamic activity owing to the synergistic effect of Type I and Type II mechanisms [32,33]. To enhance the photosensitizer solubility and bioavailability, a sustained release formulation is preferred [34]. Hyaluronic acid (HA) grafted with poly (lactic-*co*-glycolic acid) (PLGA) is a known polymer combination for fabrication of drug-loaded nanoparticles and has lately become a research hotspot due to its unique properties [35,36]. HA is a linear, anionic, biocompatible and biodegradable polysaccharide found mostly in the extracellular matrix [37]. Due to its specific affinity for the CD44 receptor [38], usually over-expressed in cancer cells, HA is an efficient encapsulation scaffold for hydrophilic drug delivery systems [39,40]. However, the loading of hydrophobic molecules in HA nanoparticles (NPs) is usually poor. To enhance it, HA is conjugated with hydrophobic moieties such as 5β-cholanic acid [41] or PLGA [42] to yield high payloads of hydrophobic chemotherapeutic drugs [43] and photosensitizers [44,45] into self-assembled HA-NPs. The latter can be selectively taken up by tumor cells through receptor-mediated endocytosis and the internalized HA-NPs can be readily degraded by the action of intracellular hyaluronidase enzymes (HASE), over-expressed by tumor cells [46], releasing the encapsulated drug.

Herein, we describe the synthesis, spectroscopic and photochemical characterization of a novel ruthenium(II)-bim complex and its subsequent encapsulation in HA-PLGA NPs (Scheme 1) for topical application in oral cancer PDT. Besides the bim ligand, two ancillary 3,4,7,8-tetramethy-1,10-phenanthroline ligands are included in the coordination sphere of the Ru(II) cation. The multiple methyl groups increase the hydrophobicity of the complex, thus improving its internalization into the cells. There are examples of physical encapsulation of Ru(II)-polypyridyl complexes into various scaffolds [47]; however, to the best of our knowledge, this is the first report of Ru(II)-loaded HA-PLGA nanoparticles for PDT. The photosensitizing NPs developed in our study exhibit high aqueous stability, low polydispersity, significant metallosensitizer encapsulation efficiency and a controlled release of the photosensitizer accelerated by hyaluronidases. We also report the evaluation of the novel Ru(II)-bim complex and its encapsulated nanoform as a possible type I/type II PDT agent on oral cancer cells under blue light activation.

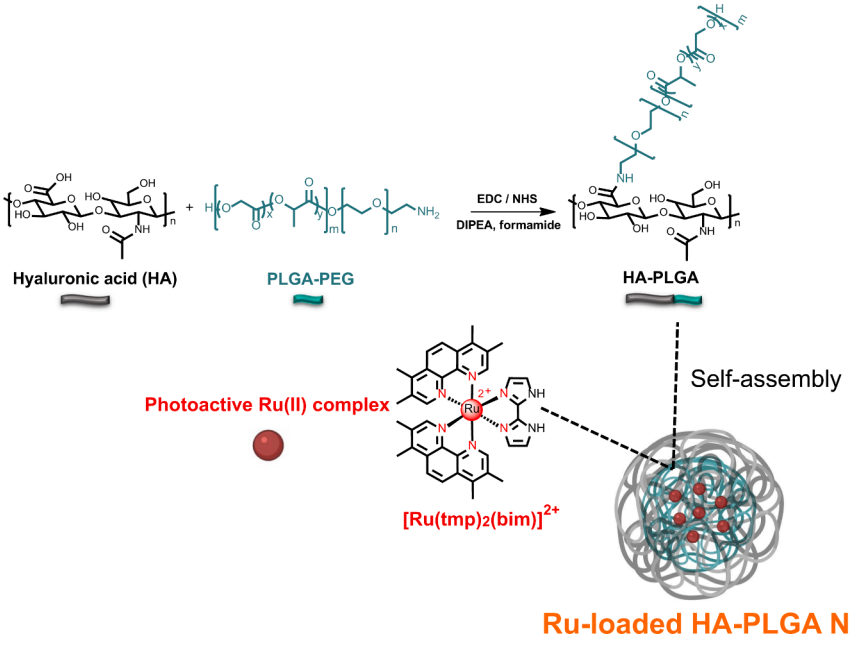


**Scheme 1.** Preparation of $[Ru(tmp)_2(bim)]^{2+}$ photosensitizer-loaded hyaluronic acid (HA)–poly(lactic-*co*-glycolic acid) (PLGA) NPs for PDT.

## 2. Materials and methods

### 2.1. Chemicals

The precursor 2,2′-biimidazole (bim) ligand and ammonium hexafluorophosphate were from Fluorochem whereas the 3,4,7,8-tetramethyl-1,10-phenanthroline (tmp) ligand was purchased from Merck. Lithium chloride and Ru(III) chloride trihydrate were from Acros Organics. Sodium hyaluronate ($2 \times 10^5$ Da) was from Lifecore Biomedical (Chaska, MN). Lyophilized hyaluronidase (Type VIII, from bovine testes, 300–1,000 U/mg), dihydroethidium (DHE), *N*,*N*-diisopropylethylamine (DIPEA), potassium dioxide, anhydrous dimethylformamide (DMF), formamide, *N*-hydroxysuccinimide (NHS), and *N*-(3-dimethylaminopropyl)-*N*′-ethylcarbodiimide hydrochloride (EDC) were from Sigma-Aldrich, and poly(L-lactide-*co*-glycolide)-*block*-poly(ethylene glycol)-amine (PLGA-PEG-$NH_2$) (Mw ~ 12,000:5,000 Da) from PolySciTech (West Lafayette, IN). Dichloromethane, methanol, dimethyl sulfoxide, 3-(4,5-dimethylthiazol-2-yl)-2,5-diphenyltetrazoliumbromide (MTT), Hoechst, MitoTracker™ Deep Red FM and LysoTracker™ Red DND-99 were purchased from ThermoFisher Scientific. Acetonitrile (MeCN) (HiPerSolv Chromanorm HPLC grade), acetone, and deuterated solvents with tetramethylsilane (TMS) as internal reference were from VWR International Eurolab. Ethylene glycol (+99 %) was from Scharlau (Sentmenat, Spain). Phosphate-buffered saline (PBS) (1X, pH 7.0) was from Corning (Corning, NY). Ultrapure water was obtained immediately before use from a Merck Direct-Q3-UV system.

### 2.2. Synthesis of *cis*-$Ru(tmp)_2Cl_2$

This precursor complex was synthesized by adapting a general protocol for the synthesis of *cis*-$[Ru(bpy)_2Cl_2]$ [48]: 87.6 mg (0.42 mmol) of Ru(III) chloride hydrate, 200 mg (0.85 mmol) of tmp, and 106 mg (2.52 mmol) of lithium chloride were dissolved in 2 mL of anhydrous DMF. A large excess of lithium chloride was added to avoid the formation of unwanted homoleptic $[Ru(tmp)_3]^{2+}$ complex. The reaction mixture was refluxed for 3 h under argon, then cooled down, and the Ru(II) complex was precipitated by addition of acetone. The resulting black-purple solid was collected by filtration and dried overnight *in vacuo* (62 % yield). UV–vis (MeOH): $\lambda^{max}$/nm ($\varepsilon/M^{-1}$ $cm^{-1}$) 500 (7540) 270 (131950).

### 2.3. Synthesis of $[Ru(tmp)_2(bim)]^{2+}$

A mixture of 120 mg (0.18 mmol) of *cis*-$Ru(tmp)_2Cl_2$ and 30 mg (0.22 mmol) of 2,2′-biimidazole was dissolved in 2 mL of ethylene glycol. The solution was refluxed for 1 h under argon. The heteroleptic Ru(II) complex was precipitated by addition of a saturated aqueous solution of ammonium hexafluorophosphate, filtered out and washed with water. The resulting red–orange solid was purified by column chromatography (silica gel; dichloromethane–methanol 9:1 v/v) (30 % yield). $^1$H NMR (300 MHz, MeCN-$d_3$, δ): 8.32 (d, $J = 5$ Hz, 4H), 8.04 (s, 2H), 7.74 (s, 2H), 7.19 (d, $J = 1.5$ Hz, 2H), 6.26 (d, $J = 1.5$ Hz, 2H), 2.83 (s, 6H), 2.72 (s, 6H), 2.44 (s, 6H), 2.18 (s, 6H). $^{13}$C NMR (300 MHz, MeCN-$d_3$, δ): 154.13, 154.12, 148.61, 147.89, 144.18, 144.03, 141.17, 135.45, 134.73, 129.97, 129.90, 129.30, 124.87, 124.84, 121.58, 18.18, 17.61, 14.93, 14.78. MS (ESI): $[M]^+$ calculated for $RuC_{38}H_{37}N_8$, 707.2; found, 707.2; $[M]^{2+}$ calculated for $RuC_{38}H_{38}N_8$, 354.1; found, 354.0. UV–vis (PBS): $\lambda^{max}$/nm ($\varepsilon/M^{-1}$ $cm^{-1}$) 460 (12711), 270 (87482).

### 2.4. Time-resolved luminescence measurements

Emission lifetime determinations were performed by single photon timing (SPT) on an Edinburgh Instruments (UK) FLS980-Xd2-T spectrometer, using a Horiba 470LH diode laser (463 nm, <1 ns pulse width), an excitation 467-nm bandpass interference filter, a 500 nm-blazed double monochromator in the emission path, and a Hamamatsu R928P photomultiplier thermoelectrically cooled at −21 °C. Due to the presence of different species in the excited stated as a result of the deprotonated forms of bim, we always report the so-called pre-exponentially weighted mean lifetime ($\tau_m = \sum_i B_i\tau_i / \sum_i B_i$) for each luminescence decay profile, calculated from the biexponential fit of the experimental points ($I_L(t) = A + \sum_1^2 B_i e^{-t/\tau_i}$).

### 2.5. Singlet oxygen luminescence measurements

Quantum yields of singlet oxygen production ($\Phi_\Delta$) were measured with an Edinburgh Instruments LP-900 laser kinetic spectrometer equipped with a frequency-tripled Nd:YAG laser (Minilite II, Continuum, CA) for excitation at 355 nm, and a Hamamatsu H10330-45 NIR PMT module for singlet oxygen emission monitoring at 1265 nm (Bentham TM300 monochromator with a 600 grooves $mm^{-1}$ NIR grating). The PMT is fitted with a 10 KΩ resistor at the signal output for proper amplification of the signal. A pyroelectric Gentec QE12LP-S-MB energy meter was employed to monitor the energy of the laser pulse, which was varied from 100 to 600 μJ $pulse^{-1}$ to avoid (partial) saturation of the $^1O_2$ emission signal and keep it in the linear region. Absorbance-matched ($A_{355} = 0.25$) solutions of $[Ru(tmp)_2(bim)]^{2+}$ and the reference photosensitizers $[Ru(dip)_3]^{2+}$ ($\Phi_\Delta = 0.94 \pm 0.07$ in air-equilibrated MeCN at room temperature measured against a 1*H*-phenalen-1-one standard in the same solvent, $\Phi_\Delta = 0.98 \pm 0.07$ [49] or $[Ru(dpds)_3]^{4-}$ ($\Phi_\Delta = 0.43 \pm 0.04$ in air equilibrated $D_2O$ at room temperature [50]) were used for the measurements. Typically, 40 laser shots were summed for each signal to improve the S/N ratio.

### 2.6. Superoxide radical anion ($O_2^{\bullet-}$) detection

The specific $O_2^{\bullet-}$ probe dihydroethidium (DHE) was used. DHE is converted by $O_2^{\bullet-}$ into 2-hydroxyethidium, a red-fluorescent product ($\lambda_{em}^{max} = 620$ nm) [51]. The $O_2^{\bullet-}$ trapping experiments used $[Ru(tmp)_2(bim)]^{2+}$ photosensitizer ($9.0 \times 10^{-6}$ mol $L^{-1}$) and DHE ($5.0 \times 10^{-6}$ mol $L^{-1}$) dissolved in air-equilibrated MeCN-$H_2O$ 1:1 (v/v). The solution was irradiated with a temperature-stabilized 25-mW 405-nm diode laser (PTG-PPMT25, Laser 2000, France) under continuous stirring. Steady-state fluorescence spectra (corrected for the instrument response) were measured with a Horiba Fluoromax-4TCSPC spectrofluorometer fitted with a red-sensitive R928 photomultiplier (Hamamatsu, Japan) and equipped with a 150-W xenon lamp. The fluorescence spectrum of 2-hydroxyethidium was recorded ($\lambda_{exc} = 520$ nm) at different irradiation times. For control purposes, the emission of DHE was measured at different irradiation times in the absence of the Ru(II) photosensitizer and in the presence of $[Ru(tmp)_2(bim)]^{2+}$ after deoxygenation with argon before irradiation.

### 2.7. Synthesis of HA-PLGA

Hyaluronic acid (HA; 40 mg, 0.2 μmol) was dissolved in formamide (2.5 mL) with gentle heating under vigorous stirring. After HA was completely dissolved, 9 mg (0.047 mmol) of EDC and 5 mg (0.05 mmol) of NHS were added at room temperature. The reaction mixture was kept under stirring for 2 h. Then, a solution of 10 mg PLGA-PEG-$NH_2$ (0.6 μmol) and DIPEA (1 μL) in 0.5 mL of formamide was added dropwise. The reaction mixture was maintained at room temperature for 24 h. Finally, it was dialyzed against water for two days (Spectra/Por® cellulose ester membrane, MWCO 100 $k_D$, Repligen, Waltham, MA) and the resulting solution was lyophilized.

### 2.8. Synthesis and characterization of the Ru-loaded HA-PLGA NPs

$[Ru(tmp)_2(bim)]^{2+}$-loaded HA-PLGA nanoparticles were prepared by dialysis (see Scheme 1) [52]. Briefly, HA-PLGA (10 mg) and $[Ru(tmp)_2(bim)]^{2+}$ (0.1 mg) were dissolved in 1 mL of 3:1 (v/v) DMSO–DMF mixture. Then, 9 mL of deionized water was added

dropwise at room temperature under stirring, followed by 20 min of sonication over an ice bath with a micro-tip sonicator (Fisher Scientific, Waltham, MA). Thereafter, the solution was dialyzed (Spectra/Por® cellulose ester membrane MWCO 3.5–5 $k_D$) against water for 24 h to remove the organic solvent. Finally, the Ru-HA-PLGA NPs were filtered through a 0.45-μm syringe filter to discard aggregates. The amount of $[Ru(tmp)_2(bim)]^{2+}$ loaded into the HA-PLGA NPs was determined by measuring the luminescence of the encapsulated photosensitizer. In brief, 1 mg of lyophilized Ru-HA-PLGA NPs were dissolved in 1 mL of DMSO, followed by sonication for 20 min. Then, the luminescence spectrum of the Ru(II) complex was recorded ($\lambda_{exc}$ = 480 nm) and compared with a calibration curve previously plotted in DMSO (1–80 μmol $L^{-1}$). A blank was measured with the unloaded HA-PLGA NPs. The hydrodynamic diameter, polydispersity and zeta potential of the NPs were determined by a Zetasizer Nano ZS dynamic light scattering apparatus (Malvern Instruments, Houston, TX). The NP size and morphology were also evaluated with a Philips CM10 Transmission Electron Microscopy (TSS Microscopy, Hillsboro, OR).

### 2.9. Drug release assay

Ru-HA-PLGA NPs in PBS (7.0 mg $mL^{-1}$) were placed in a dialysis bag (Spectra/Por® cellulose ester membrane, MWCO 100 $k_D$, Repligen, Waltham, MA) and immersed in 9 mL phosphate buffer (PBS, pH 7.0) in the presence of 0 or 150 units $mL^{-1}$ of hyaluronidase (HASE) at 37 °C under mild shaking. At different time points, 200 μL aliquots of the media were withdrawn and the same volume was replaced with an equal volume of PBS with similar concentration of HASE to maintain a constant sink condition. The $[Ru(tmp)_2(bim)]^{2+}$ release from Ru-loaded-HA-PLGA NPs was determined by measuring the luminescence of the aliquots ($\lambda_{exc}$ = 480 nm) and the corresponding calibration curve in PBS (1–80 μmol $L^{-1}$).

### 2.10. Cell culture

The human buccal carcinoma cell line TR146 was obtained from ECACC (European Collection of Authenticated Cell Cultures). The human oral squamous cell carcinoma line (CAL27) and the Chinese hamster ovarian cell line (CHO) were obtained from ATCC, Manassas, VA and cultured as mentioned previously [53,54]. Briefly, TR146 cells were cultured in DMEM/F12 medium (Fisher Scientific, Waltham, MA), CAL27 cells were cultured in DMEM (Fisher Scientific, Waltham, MA) and CHO cells were cultured in F-12 K media (ThermoFisher Scientific, Waltham, MA), respectively. All cell culture media were supplemented with 10 % FBS and antibiotic mixture containing penicillin (100 I.U./mL) and streptomycin (100 μg $mL^{-1}$) (Mediatech, Manassas, VA), and incubated at 37 °C in a 5 % $CO_2$ atmosphere.

### 2.11. Cellular uptake

TR146 cells were seeded in a 6-well plate at a cell density of 200,000 cells per well in 2000 μL of media and allowed to grow overnight. Thereafter, the cells were treated with $[Ru(tmp)_2(bim)]^{2+}$ (0.25 μmol $L^{-1}$) and Ru-HA-PLGA NPs (1.0 μmol $L^{-1}$ $[Ru(tmp)_2(bim)]^{2+}$ equivalent). At different time points (3 h, 6 h, 12 h and 24 h), the medium was removed, and the cells were washed with PBS (2 × 2.0 mL), trypsinized, and analyzed with a flow cytometer (BD FACSAria™ Cell Sorting System, Biosciences).

### 2.12. Colocalization assay

Colocalization analysis was performed as reported previously [53]. Briefly, TR146 cells were plated in 35-mm glass bottom dishes (Cellvis, Mountain View, CA) at a cell density of 50,000 cells per dish in 2000 μL of media and allowed to grow overnight at 37 °C under 5 % $CO_2$. Cells were treated with $[Ru(tmp)_2(bim)]^{2+}$ complex (0.25 μmol $L^{-1}$) and Ru-HA-PLGA NPs (1.0 μmol $L^{-1}$ $[Ru(tmp)_2(bim)]^{2+}$ equivalent) for 12 h and incubated with MitoTracker® Red for 30 min prior to fixation. Cells were then washed with PBS (2 × 2.0 mL), fixed with 4 % paraformaldehyde solution in PBS for 15 min, washed with PBS (2 × 2.0 mL) and counterstained with Hoechst at a concentration of 1 μg $mL^{-1}$. Cells were visualized using an Olympus FLUOVIEW FV1000 confocal laser scanning microscope (Olympus America, Center Valley, PA). Image analysis was performed using Image-J software (National Institute of Health, Bethesda, MD).

### 2.13. In vitro cytotoxicity

Dark and light-induced cytotoxicity was assessed by the colorimetric MTT assay. TR146, CAL27 and CHO cells were plated in triplicates in 96-well plates at a density of 5,000 cells per well in 200 μL of media and allowed to grow. For assessing dark cytotoxicity of the compounds, cells were treated with increasing concentrations (0.25 to 50 μmol $L^{-1}$) of $[Ru(tmp)_2(bim)]^{2+}$ or Ru-HA-PLGA NPs for 12 h. For phototoxicity assessment, cells were treated with $[Ru(tmp)_2(bim)]^{2+}$ (0.25 μmol $L^{-1}$) or Ru-HA-PLGA NPs (1.0 μmol $L^{-1}$ $Ru(tmp)_2(bim)]^{2+}$ equivalent) for 12 h. After incubation, the culture media was replaced with fresh medium, and irradiated with a 470 nm 70 mW $cm^{-2}$ (min) mounted LED (M470L3, Thorlabs, Newton, NJ) with increasing radiant energy fluences (2.5, 5, 10, 25 and 50 J $cm^{-2}$) and further incubated in dark at 37 °C under 5 % $CO_2$ for 24 h. Finally, a freshly prepared MTT solution (0.25 mg $mL^{-1}$) in culture media was added to each well and incubated at 37 °C for 30 min. After removal of the medium containing MTT, the formazan crystals formed by viable cells were dissolved in DMSO (200 μL) and the absorbance was recorded at 570 nm using a SpectraMax M5 multimode microplate reader (Molecular Devices, San Jose, CA). Cytotoxicity (%) for different treatment groups was calculated with respect to the MTT assay results for the untreated control.

### 2.14. Statistical analysis

Statistical analysis was performed using GraphPad Prism (GraphPad Software). All data are presented as mean ± SEM, unless otherwise stated. Parametric test (one-way ANOVA) was used for phototoxicity studies in Fig. 5 and Supplementary Fig. S14 to calculate statistically significant differences between multiple treatment groups. The Brown–Forsythe test ($\alpha = 0.05$) was applied to data sets with $n \geq 3$ to test for homogeneity of variance. During the entire analysis, no exclusion test was performed, and data points were not excluded from the analysis.

## 3. Results and discussion

With the aim of maximizing the cellular uptake and the photogeneration of superoxide anion, a series of Ru(II)-complexes containing a single 2,2′-biimidazole (bim) ligand were prepared by chelating two 2,2′-bypiridine (bpy), 1,10-phenantroline (phen) or 3,4,7,8-tetramethyl-1,10-phenanthroline (tmp) as ancillary ligands in the pseudooctahedral Ru(II) coordination sphere, following a reported procedure [28]. The uptake of the dyes in TR146 cells was studied by incubating the dyes with the cells for 24 h, followed by analysis using flow cytometry. As shown in Fig. S1 (Supporting Information), a strong luminescence signal was observed when the cells were treated with the hydrophobic Ru(II) complex ($[Ru(tmp)_2(bim)]^{2+}$). However, a two- order of magnitude lower signal was observed for the other two hydrophilic Ru(II)-bim dyes. These results are in agreement with literature results that show higher uptake for hydrophobic Ru(II) complexes [55,56]. Therefore, $[Ru(tmp)_2(bim)]^{2+}$ was selected as potential candidate for type I / type II PDT.

### 3.1. Synthesis of the $[Ru(tmp)_2(bim)]^{2+}$ photosensitizer

The chemical structure and the synthesis procedure of the heteroleptic complex $[Ru(tmp)_2(bim)]^{2+}$ containing two 3,4,7,8-tetramethyl-1,10-phenanthroline (tmp) and one 2,2′-biimidazole (bim) ligands is depicted in Fig. S2 (Supporting Information). Figs. S3–S5 (Supporting Information) document the spectroscopic characterization of $[Ru(tmp)_2(bim)]^{2+}$, isolated as $PF_6^-$ salt, by $^1H$ NMR, $^{13}C$ NMR and ESI-MS. The four methyl groups on the phenanthroline moiety significantly increase the lipophilicity of the cationic photosensitizer reducing its solubility in water.

### 3.2. UV-light triggered ROS generation

To determine whether or not molecular oxygen had a significant influence on the luminescence of $[Ru(tmp)_2(bim)]^{2+}$, we measured the luminescence lifetimes in air-equilibrated and deoxygenated acetonitrile (MeCN) under 463 nm excitation. $[Ru(tmp)_2(bim)]^{2+}$ showed a pre-exponentially weighted average lifetime ($\tau_m$, see Experimental section) of 18 ns and 104 ns in aerated and $^3O_2$-free MeCN, respectively. These results confirm that molecular oxygen quenches the (triplet) excited state of the complex. Therefore, we evaluated the ability of $[Ru(tmp)_2(bim)]^{2+}$ to photosensitize the production of singlet oxygen ($^1O_2$) by monitoring the $^1O_2$ emission decay at 1265 nm in air-equilibrated solution (Fig. 1a). The luminescence of the unquenched metal-to-ligand charge transfer triplet ($^3$MLCT) excited state is also visible at 1265 nm [50]. The production of singlet oxygen ($^1O_2$) was also measured in $D_2O$ (used as a surrogate of $H_2O$ as the emission of $^1O_2$ in $H_2O$ is extremely weak [57]). The quantum yield of $^1O_2$ production ($\Phi_\Delta$) was determined by using two reference photosensitizers of the same family namely, tris(4,7-diphenyl-1,10-phenanthroline)ruthenium(II) dication ($[Ru(dip)_3]^{2+}$, $\Phi_\Delta = 0.94 \pm 0.07$) in aerated MeCN, and tris [(1,10-phenanthroline-4,7-diyl)-bis(benzenesulfonato)]ruthenate ($[Ru(dpds)_3]^{4-}$, $\Phi_\Delta = 0.43 \pm 0.04$) in aerated $D_2O$ solution [50]. $\Phi_\Delta$ for $[Ru(tmp)_2(bim)]^{2+}$ (Fig. S6, Supporting Information) was found to be 0.22 ± 0.05 in aerated MeCN. However, $^1O_2$ generation in aqueous environment was negligible ($\Phi_\Delta < 0.01$) possibly due to ca. 10-fold lower oxygen concentration in water as compared to organic solvents, taking into account the similar excited state lifetime in those solvents (95 ns). The analogous homoleptic complex $[Ru(tmp)_3]^{2+}$ exhibits a $\Phi_\Delta$ value of 0.80 ± 0.04 in aerated acetonitrile. This higher $\Phi_\Delta$ is presumably due to the longer excited-state lifetime of $[Ru(tmp)_3]^{2+}$(463 ns) than that of $[Ru(tmp)_2(bim)]^{2+}$ (103 ns) in deoxygenated MeCN, since the excited state oxidation potential of those complexes is identical (–1.03 V/NHE and –1.05 V/NHE, respectively). This logical result is a consequence of the higher energy of π* orbital of bim due to its π-excessive electron density compared to phenanthroline. The excited state oxidation potentials ($E^{3+/2+*}$) have been calculated from the measured ground state oxidation potentials (1.04 V/NHE and 0.86 V/NHE, respectively, Fig. S7a, Supporting Information) and the approximate energy of the π* → $d_{t2g}$ transition (600 nm and 650 nm, equivalent to 2.06 eV and 1.90 eV, respectively, Fig. S7b, Supporting Information,). The high energy of

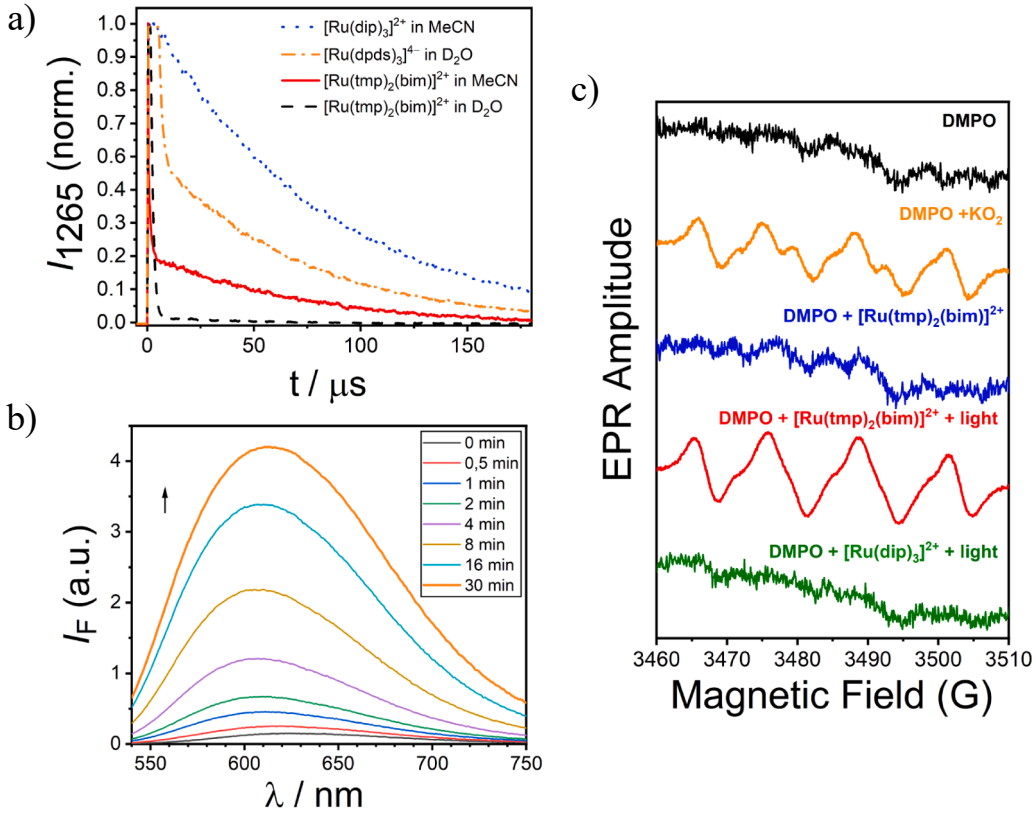


**Fig. 1.** a) Decay of the $^1O_2$ luminescence at 1265 nm upon excitation with 3-ns 0.5-Hz 355-nm Nd:YAG laser pulses (the depicted decays are the sum of 40 pulses) of solutions of $[Ru(tmp)_2(bim)]^{2+}$ in air-equilibrated MeCN (red solid line; $\tau = 77 \pm 3$ μs) or $D_2O$ (black dashed line; $\tau = 67 \pm 1$ μs) ($A_{355} = 0.25$). The quantum yield of singlet oxygen production ($\Phi_\Delta$) was measured using absorbance-matched solutions of the reference photosensitizers $[Ru(dip)_3]^{2+}$ in MeCN (blue dotted line; $\Phi_\Delta = 0.94 \pm 0.07$) or $[Ru(dpds)_3]^{4-}$ in $D_2O$ (orange dashed-dotted line; $\Phi_\Delta = 0.43 \pm 0.04$) (see text for the photosensitizer names). b) Fluorescence spectrum of $HOE^+$ ($\lambda_{exc} = 520$ nm) under continuous irradiation with a 50-mW 405-nm diode laser of $[Ru(tmp)_2(bim)]^{2+}$ (9.0 μmol $L^{-1}$) in the presence of DHE (50.0 μmol $L^{-1}$), in 1:1 (v/v) MeCN-water. c) EPR spectra in 1:1 (v/v) MeCN-water solution of (from top to bottom) DMPO (44.2 mmol $L^{-1}$), DMPO with excess of $KO_2$, DMPO with 10.0 μmol $L^{-1}$ of $[Ru(tmp)_2(bim)]^{2+}$, DMPO with 10.0 μmol $L^{-1}$ of $[Ru(tmp)_2(bim)]^{2+}$ after 300-s illumination, and DMPO with 2.1 mmol $L^{-1}$ of $[Ru(dip)_3]^{2+}$ after 300-s illumination.

the TMP and bim π* orbitals will favor the superoxide anion $O_2^{\bullet-}$ generation by photoinduced electron transfer quenching from *[Ru(tmp)$_2$(bim)]$^{2+}$ to $^3O_2$ ($E^{0/-}$ = –0.33 V/NHE [57]) [31].

To confirm the production of $O_2^{\bullet-}$, we used dihydroethidium (DHE) which specifically reacts with $O_2^{\bullet-}$ [51]. The latter is a non-fluorescent molecule that can be oxidized by superoxide yielding the red-fluorescent product 2-hydroxyethidium ($HOE^+$, $\lambda_{em}^{max}$ = 620 nm in water) [58,59]. A [Ru(tmp)$_2$(bim)]$^{2+}$ solution irradiated in the presence of DHE with a 405-nm diode laser (a wavelength where the photosensitizer dye has a high absorption but that of DHE and the $HOE^+$ being generated is negligible (Fig. S8a, Supporting information), showed a dramatic increase in its fluorescence (Fig. 1b) as compared to when it is excited at 520 nm (a wavelength where only $HOE^+$ has a significant absorption, Fig. S8a, Supporting information). The fluorescence intensity decreased significantly when DHE was irradiated for the same period of time in the absence of photosensitizer or in the presence of the latter but in deoxygenated solution (sparged with argon before irradiation; Fig. S8b, Supporting information).

We further proved the generation of $O_2^{\bullet-}$ by electron paramagnetic resonance (EPR) spectroscopy using 5,5-dimethyl-1-pyrroline-*N*-oxide (DMPO) as the spin-trap agent [60]. As shown in Fig. 1c, no EPR signals were observed when DMPO and [Ru(tmp)$_2$(bim)]$^{2+}$ were incubated in dark. In contrast, after 5 min illumination, a characteristic paramagnetic DMPO-$O_2^{\bullet-}$ adduct was observed with an EPR spectrum similar to that of potassium superoxide ($KO_2$) in DMPO solution. For comparison, the same experiment was carried out in the presence of the longer lived $^3$[Ru(dip)$_3$]$^{2+}$ ($\tau_0$ = 6 μs) [50], a photosensitizer dye which exclusively generates $^1O_2$ (see above). In this case, no EPR signal was observed after irradiation (Fig. 1c), thus confirming the photogeneration of $O_2^{\bullet-}$ by [Ru(tmp)$_2$(bim)]$^{2+}$.

### 3.3. Preparation and characterization of Ru-HA-PLGA NPs

To increase the bioavailability of the hydrophobic [Ru(tmp)$_2$(bim)]$^{2+}$, it was encapsulated in HA-PLGA nanoparticles. HA-PLGA nanoparticles have been previously demonstrated to efficiently encapsulate hydrophobic drugs in the PLGA core while the hydrophilic HA shell assists in stabilizing the nanoparticles in aqueous environments [36,39]. The procedure followed for the synthesis of the Ru-loaded HA-PLGA NPs is depicted in Scheme 1. Briefly, an amine-terminated PEGylated PLGA (PLGA-PEG-$NH_2$) was conjugated to hyaluronic acid by EDC/NHS coupling. The successful chemical functionalization of HA was confirmed by $^1$H NMR (Fig. S9, Supporting Information). The presence of PLGA chains is essential for promoting self-assembly and encapsulation of the hydrophobic [Ru(tmp)$_2$(bim)]$^{2+}$. Encapsulation of the dye was carried out firstly by dispersing both entities, the HA-PLGA scaffold and [Ru(tmp)$_2$(bim)]$^{2+}$, in a DMF-DMSO (3:1 v/v) mixture followed by slow addition of deionized water until the solution turned turbid. In order to facilitate the diffusion of dye molecules into the polymer core, the suspension was ultrasonicated and, finally, the

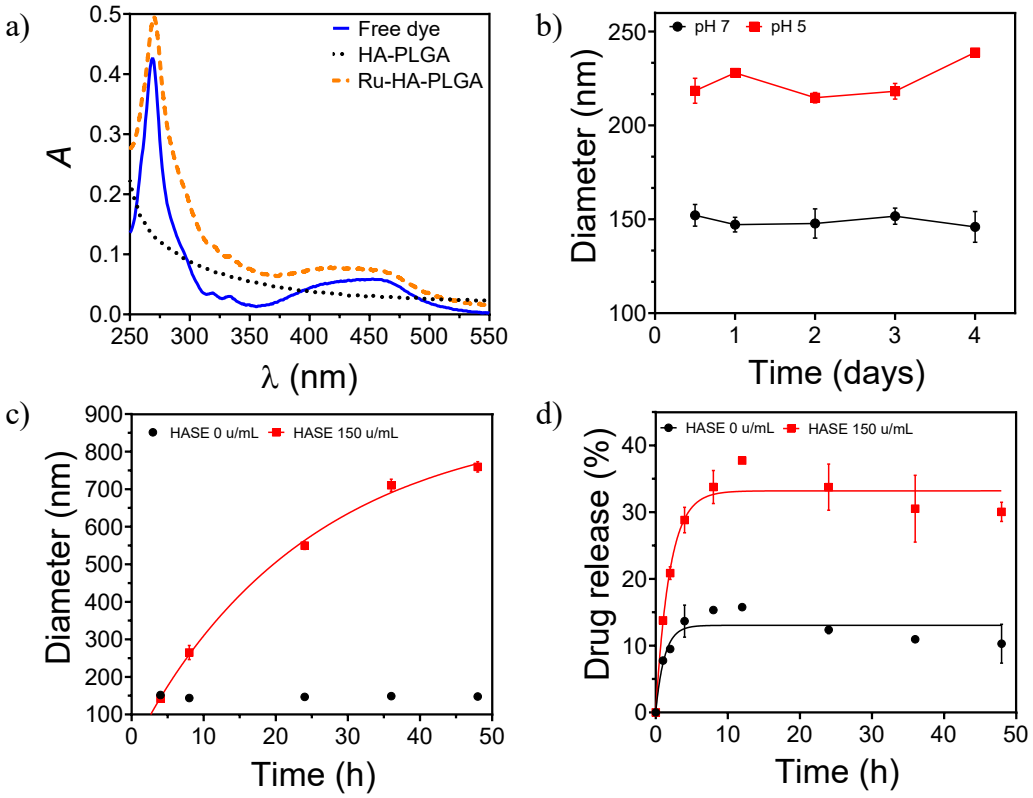


**Fig. 2.** a) UV–vis absorption spectra of the [Ru(tmp)$_2$(bim)]$^{2+}$ (7.0 × 10$^{-6}$ mol L$^{-1}$) (blue solid line), HA-PLGA NPs (black dotted line), and Ru-HA-PLGA NPs in water. The Ru-HA-PLGA NPs showed absorption bands characteristic of [Ru(tmp)$_2$(bim)]$^{2+}$. b) Evolution of the Ru-HA-PLGA particle size in PBS (pH = 7.0) and acetate buffer (pH = 5.0) at 37 °C for 4 days, as monitored by DLS. While the particle size at pH 5 was found to be higher, there was no significant change in size, over a period of 4 days, under both the conditions. Data are presented as mean ± S.D ($n \geq 3$). c) Evolution of the Ru-HA-PLGA particle size in PBS (pH = 7.0) at 37 °C for 48 h, in the absence and in the presence of 150 units mL$^{-1}$ of hyaluronidase (HASE), monitored by DLS. Non-linear fit (red curve, $r^2$ = 0.998) to the exponential association function $f(x) = y_{max} \times (1 - e^{-kx})$ with the following parameters: $y_{max}$ = (874 ± 34) nm; $k$ = (40 ± 4) × 10$^{-3}$ h$^{-1}$ is shown for the HASE treated Ru-HA-PLGA NPs. d) Release of the [Ru(tmp)$_2$(bim)]$^{2+}$ from the Ru-HA-PLGA NPs, as studied for 48 h, in the absence and presence of 150 units mL$^{-1}$ of HASE in PBS (pH = 7.0) at 37 °C. Non-linear fit to an exponential association function $f(x) = y_{max} \times (1 - e^{-kx})$, defined by the following parameters: $y_{max}$ = (33 ± 1) nm and $k$ = (51 ± 7) × 10$^{-2}$ h$^{-1}$ ($r^2$ = 0.965) and $y_{max}$ = (13.1 ± 0.8) nm and $k$ = (0.8 ± 0.3) h$^{-1}$ ($r^2$ = 0.849) are shown as red and black lines, respectively.

obtained nanoparticles were subjected to dialysis for removing non-encapsulated photosensitizer molecules and the DMF-DMSO solvent mixture, as reported previously [52]. Once the Ru-HA-PLGA NPs were prepared their absorption spectrum was recorded and compared to that of the free complex in aqueous solution (Fig. 2a). The characteristic Ru (II)-broad absorption band at 470 nm assigned to an allowed MLCT transition was also observed in the Ru-HA-PLGA NPs, suggesting that the spectroscopic properties of the photosensitizer were not affected after encapsulation.

Transmission electron microscopy (TEM) images confirmed the successful synthesis of the HA-PLGA NPs (Fig. S10, Supporting Information) and their properties are depicted in Table 1. While the diameter of the NPs in the absence of the photosensitizer, as analyzed by TEM, was 50 nm, a larger hydrodynamic diameter was observed by dynamic light scattering (143 ± 2 nm; Table 1). This significant difference might be ascribed to shrinkage of the NPs due to dehydration during sample preparation and TEM imaging, performed under high vacuum, as has been reported previously for nanoparticles synthesized with hydrophilic polymers [61]. The addition of 0.1 mg of $[Ru(tmp)_2(bim)]^{2+}$ per 10 mg of HA-PLGA resulted in a slight increase in size to 152 ± 6 nm (DLS). Preparations with higher amounts of $[Ru(tmp)_2(bim)]^{2+}$ led to an increase in nanoparticle size (>200 nm) (data not shown). All the nanoformulations described above showed a negative zeta potential (Table 1) demonstrating the presence of the ionized HA on their surface, at pH 7.0. PLGA nanoparticles synthesized from PLGA-PEG-$NH_2$ showed a lower zeta-potential (0 to −2 mV), further confirming the presence of HA on the surface on the nanoparticles. This is in agreement with previous studies where the PEGylated PLGA has been reported to have close to neutral zeta-potential [62]. For further studies, Ru-HA-PLGA NPs prepared with 0.1 mg Ru(II) complex per 10 mg HA-PLGA were used as they showed the "ideal" size (diameter < 200 nm) required for in vivo applications [34]. The photosensitizer encapsulation efficiency and the loading content in NPs were determined by luminescence analysis of the extracted complex after generating a calibration curve in DMSO. A 70 ± 9 % encapsulation efficiency of $[Ru(tmp)_2(bim)]^{2+}$ in the HA-PLGA NPs was achieved, highlighting the high efficiency of the preparation procedure, as compared to previous studies which have reported lower encapsulation efficiencies, ranging from 10 to 45 % [63,64].

To evaluate the stability of the Ru-HA-PLGA NPs, the NPs were suspended in PBS with pH 7.0 and in acetate buffer with 5.0, respectively, for 4 days at 37 °C, to imitate healthy tissue and acidic microenvironment of the tumor. Fig. 2b shows that the environmental pH significantly alters the NP size, and a larger diameter was observed in acidic medium (152 ± 6 and 219 ± 7 nm at pH 7.0 and pH 5.0, respectively). This is not without precedent for HA-PLGA NPs [52], and is due to the protonation of carboxylic acid groups in HA at lower pH values leading to decrease in electrostatic repulsion and hence aggregation of the NPs. Despite this effect, the NP size did not change significantly for 4 days, demonstrating good physical stability in that pH range. This increased stability may be ascribed to the presence of the biodegradable PLGA chemically conjugated to the HA backbone [35].

The degradation of the HA-PLGA scaffold in the presence of hyaluronidase enzyme (HASE) and the release of the $[Ru(tmp)_2(bim)]^{2+}$, was also evaluated. Upon incubation with HASE, the mean diameter dramatically increased to 615 ± 11 nm within 48 h (Fig. 2c), suggesting partial HA degradation and nanoparticle loosening, as reported previously [52]. These results are in good agreement with the drug release profile measured in the presence of HASE (Fig. 2d): in the first 12 h, 12.4 ± 0.6 % of $[Ru(tmp)_2(bim)]^{2+}$ was released under physiological conditions. However, the release rate of $[Ru(tmp)_2(bim)]^{2+}$ from the NPs was much higher in the presence of HASE (38 ± 1 %). Both, the degradation and drug release curves, were successfully fitted to an exponential association function (Fig. 2c and 2d). While conventional nanoformulations might undergo hydrolytic degradation, the NPs developed in our study rely on the action of hyaluronidase enzymes overexpressed and secreted by cancer cells which could facilitate $[Ru(tmp)_2(bim)]^{2+}$ release in the tumor microenvironment and in the tumor cells thereby enhancing tumor specificity and activity [65].

### 3.4. Cellular uptake and subcellular localization

The intracellular uptake and subcellular localization of $[Ru(tmp)_2(bim)]^{2+}$ and the Ru-HA-PLGA NPs in TR146 cells were analyzed by flow cytometry (Fig. 3) and confocal fluorescence microscopy (Fig. S11, Supporting Information). A gradual increase in the intracellular $[Ru(tmp)_2(bim)]^{2+}$ luminescence intensity was observed, for both the $[Ru(tmp)_2(bim)]^{2+}$ treated and Ru-HA-PLGA NP treated cells over the 24 h incubation period. To further investigate if the internalization of Ru-HA-PLGA NPs is mediated by the CD44 receptor, a competitive assay with free HA was performed and analyzed by flow cytometry. As shown in Fig. S12 (Supporting Information), a 22 % reduction ($P < 0.01$) in the cellular uptake of Ru-HA-PLGA NPs was observed in the presence

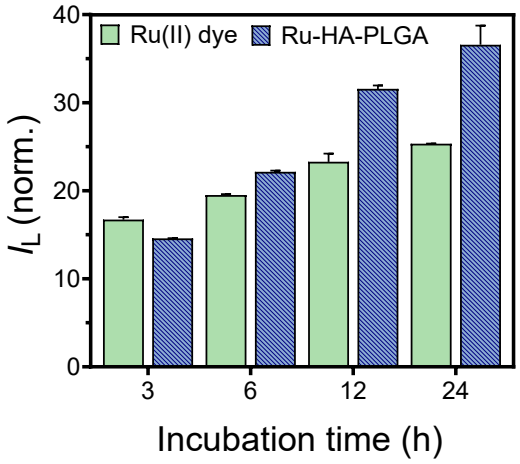


**Fig. 3.** Flow cytometry analysis of TR146 cells treated with free $[Ru(tmp)_2(bim)]^{2+}$ (0.25 μmol $L^{-1}$) or Ru-HA-PLGA NPs (1.0 μmol $L^{-1}$ of $[Ru(tmp)_2(bim)]^{2+}$ equivalent) performed at different times. Luminescence values are normalized to the non-treated control for the respective time points. Data are presented as mean ± S.D ($n \geq 3$).

**Table 1**
Physico-chemical characterization of Ru-HA-PLGA NPs.

| Ru complex/ HA-PLGA (mg/mg) | TEM mean diameter (nm) | DLS mean diameter (nm)[a] | PDI[a,b] | ζ (mV)[a] | Ru complex encapsulation efficiency (%)[a] | Ru complex content (%)[c] |
|---|---|---|---|---|---|---|
| 0/10 | 50 ± 10 | 143 ± 2 | 0.07 ± 0.02 | –9.8 ± 0.6 | – | – |
| 0.1/10 | 70 ± 20 | 152 ± 6 | 0.12 ± 0.05 | –9 ± 1 | 70 ± 9 | 0.15 ± 0.03 |

[a] In phosphate buffer (1X) at pH 7.0.
[b] Polydispersity index.
[c] By weight.

of free HA. However, the decrease in luminescence was observed to be just 10 % ($P < 0.05$) when the cells were treated with [Ru(tmp)$_2$(bim)]$^{2+}$ in the presence of free HA. These results suggest that the Ru-HA-PLGA NPs are being taken up by TR146 cells through CD44 receptor-mediated endocytosis [52]. The latter highlights the CD44 targeting potential of Ru-HA-PLGA NPs.

As shown in Fig. 3, a strong [Ru(tmp)$_2$(bim)]$^{2+}$ luminescence signal was observed even for short incubation times. The high lipophilicity and the cationic character of the [Ru(tmp)$_2$(bim)]$^{2+}$ determines its rapid uptake and, possibly, its intracellular localization. For instance, some reports have demonstrated that those features lead to an increased accumulation of [Ru(tmp)$_2$(bim)]$^{2+}$ in the mitochondria [66]. Therefore, confocal fluorescence microscopy with commercial MitoTracker® Red was performed to evaluate the accumulation of the dye and the Ru-HA-PLGA NPs in mitochondria. The fluorescence emission from the [Ru(tmp)$_2$(bim)]$^{2+}$ complex, depicted in Fig. 4, overlaps with the fluorescence of MitoTracker® Red, suggesting mitochondrial co-localization. To corroborate it, the Pearson's correlation coefficient ($r$) was determined for the Ru(II) dye (0.73) and the Ru-HA-PLGA NPs (0.64). In contrast, a significantly lower co-localization ($r = 0.35$ and 0.40, respectively) was observed with LysoTracker® (Fig. S13, Supporting Information). These results confirm that [Ru(tmp)$_2$(bim)]$^{2+}$ preferentially accumulates in the mitochondria even when encapsulated in the HA-PLGA NPs. This is of special interest due to the key role that mitochondria plays in the cells including ATP generation, regulation of cell proliferation and apoptosis [67]. In this context, several studies have confirmed the enhancement of apoptosis by mitochondria-targeted PDT through photoinactivation of antiapoptotic proteins (Bcl2 and Bcl-xL) [68–73], thus underlining the promising potential of [Ru(tmp)$_2$(bim)]$^{2+}$ as PDT agent.

### 3.5. Cytotoxicity of [Ru(tmp)$_2$(bim)]$^{2+}$ and Ru-HA-PLGA NPs

The in vitro dark cytotoxicity of [Ru(tmp)$_2$(bim)]$^{2+}$ and Ru-HA-PLGA NPs was firstly evaluated on TR146 cells. Fig. 5a shows the cytotoxicity (%) with increasing concentrations of free [Ru(tmp)$_2$(bim)]$^{2+}$ and Ru-HA-PLGA NPs, as determined by the MTT cell viability assay. Ru-HA-PLGA NPs displayed a significantly lower cytotoxicity throughout the investigated concentration range with 12 h of incubation. $IC_{50}$ values of 0.65 ± 0.14 μmol L$^{-1}$ and 2.7 ± 0.3 μmol L$^{-1}$ were measured in the dark for [Ru(tmp)$_2$(bim)]$^{2+}$ and the Ru-HA-PLGA NPs, respectively. These values are lower than those observed under similar conditions for other Ru(II) polypyridyl complexes, for which typical $IC_{50}$ values in the range of 10 to > 100 μmol L$^{-1}$ have been reported [74,75]. The higher dark toxicity of [Ru(tmp)$_2$(bim)]$^{2+}$ might be attributed to the biimidazole ligand, that has been shown to confer cytotoxicity to the metal complexes [24,28,29]. The lower toxicity of the Ru-HA-PLGA NPs suggests improved biocompatibility when encapsulated into the hydrophobic core of the PLGA-HA formulation. It can therefore be concluded that the encapsulation in HA-PLGA NPs increases the stability of [Ru(tmp)$_2$(bim)]$^{2+}$, enhancing its circulation time and releasing it specifically in the tumor microenvironment by the action of HASE, thereby significantly reducing off target effects.

Significant cytotoxicity was observed when the TR146 cells, incubated with the free and NP-encapsulated photosensitizer, were irradiated with blue light (470 nm) at radiant energy fluences ranging from 2.5 to 50 J cm$^{-2}$ (Fig. 5b). No significant cytotoxicity was detected when the TR146 cells were exposed to the highest light dose in the absence of the photosensitizer. A significant cytotoxicity ($P < 0.0001$) was observed even when the lowest fluence (2.5 J cm$^{-2}$) was applied. Interestingly, when a 50 J cm$^{-2}$ fluence was used, a 93 ± 2 % cell killing was measured, underlying the photoactivity of the photosensitizer and its nanoformulation. The notable phototoxicity of [Ru(tmp)$_2$(bim)]$^{2+}$ and the Ru-HA-PLGA NPs might be attributed to their accumulation in the mitochondria and possibly a combined Type I/Type II photosensitization. This fact allows us to work at sub-μM photosensitizer concentration, a value 10- to 100-fold lower than those of other Ru(II) polypyridyl complexes reported in the literature [75,76]. We further investigated the cytotoxicity of [Ru(tmp)$_2$(bim)]$^{2+}$ in another oral cancer cell line (CAL27) and in a non-cancerous cell line (CHO) (see Fig. S14, Supporting Information). While more than a 65 % cell killing was measured for CAL27 or TR146 cell lines when a low fluence (10.0 J cm$^{-2}$) was applied, only 27 ± 4 % toxicity was observed for the non-cancerous CHO cell line, thus revealing a preferential accumulation and toxicity of the sensitizer in malignant cells.

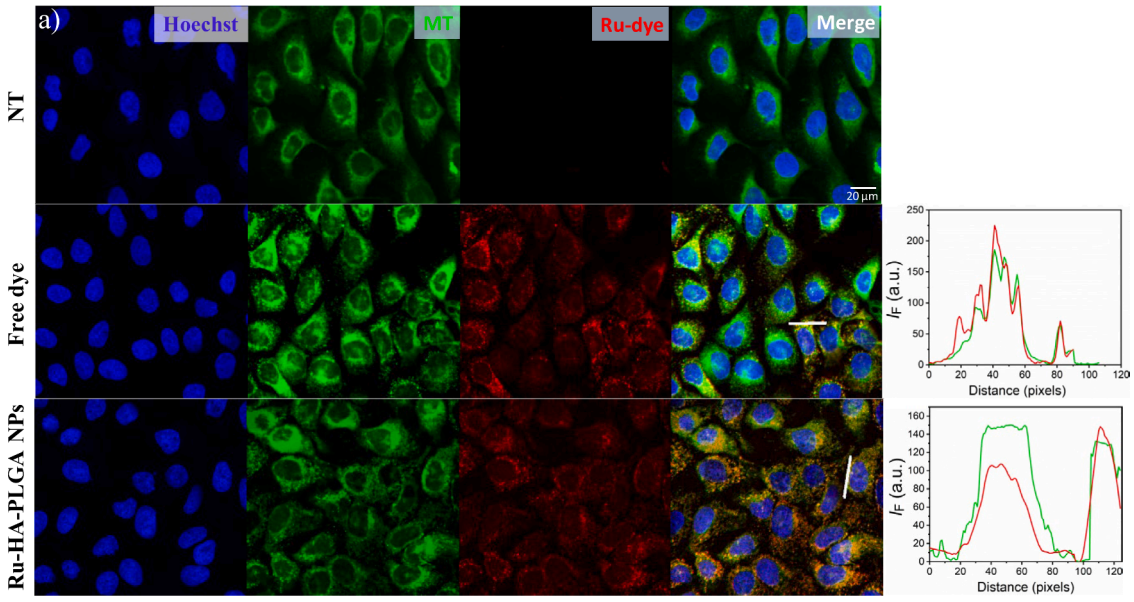


**Fig. 4.** Confocal microscopy analysis of subcellular localization of [Ru(tmp)$_2$(bim)]$^{2+}$ dye and Ru-HA-PLGA NPs in TR146 cells. a) non-treated TR146 cells (NT); b) TR146 cells treated with the [Ru(tmp)$_2$(bim)]$^{2+}$ (0.25 μmol L$^{-1}$); c) TR146 cells treated with Ru-HA-PLGA NPs (1.0 μmol L$^{-1}$ [Ru(tmp)$_2$(bim)]$^{2+}$ equivalent). Right: Fluorescence intensity profile plots were generated to study colocalization along the white line on the merged images. Nuclear staining (Hoechst) (blue); Mitochondria staining (green); [Ru(tmp)$_2$(bim)]$^{2+}$ (red). Incubation time, 24 h; scale bar, 20 μm.

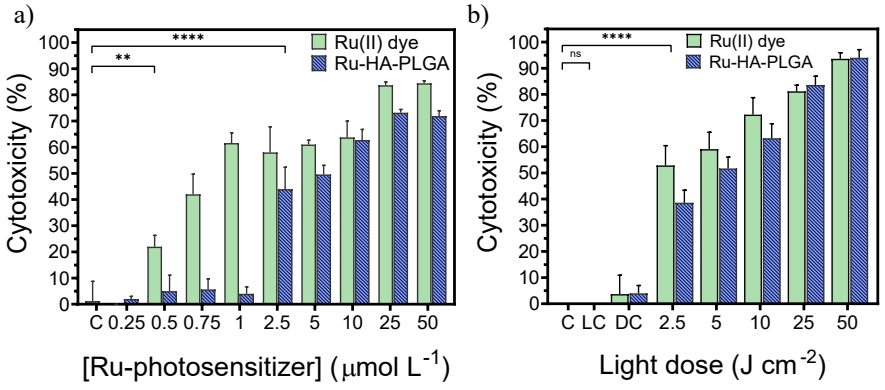


**Fig. 5.** a) Cytotoxicity (%) of $[Ru(tmp)_2(bim)]^{2+}$ and Ru-HA-PLGA NPs on TR146 cells in the dark. Data are presented as mean ± S.D ($n \geq 3$), analyzed using one-way ANOVA. P-values < 0.05 were considered to be significant and are indicated by asterisks as follows: **P < 0.01 and ****P < 0.0001. b) Cytotoxicity (%) of the non-encapsulated (0.25 μmol $L^{-1}$) and encapsulated (1.0 μmol $L^{-1}$) photosensitizer on TR146 cells upon irradiation with different radiant energy fluences (470 nm LED, 70 mW/$cm^2$). Cytotoxicity was evaluated by the MTT assay at 24 h after irradiation. Cytotoxicity (%) was calculated with respect to the untreated control. Data are presented as mean ± S.D ($n \geq 3$), analyzed using one-way ANOVA. P-values < 0.05 were considered to be significant and are indicated by asterisks as follows: $^{ns}P > 0.05$ and ****P < 0.0001.

## 4. Conclusions

A novel ruthenium(II) complex containing 2,2′-biimidazole and tetramethylated phenanthroline was synthesized as a potential PDT agent for oral cancer management. This complex has the uncommon ability to simultaneously photosensitize the generation of $^1O_2$ and $O_2^{\bullet-}$ reactive oxygen species, through type I and II PDT, upon blue light irradiation. Superoxide generation is a consequence of the π-rich character of the bim ligand, that raises the HOMO of the photoexcited dye promoting electron transfer to nearby $O_2$. The high lipophilicity of the cationic photosensitizer leads to an increased intracellular uptake, with preferential accumulation in the mitochondria. The uptake selectivity could be further improved by encapsulating the Ru(II) dye into hyaluronic acid–poly(lactic-*co*-glycolic acid) nanoparticles targeting the overexpressed hyaluronic acid receptors (CD44) in different tumor types. We demonstrate successful encapsulation of the Ru(II) complex without loss of photodynamic activity of the photosensitizer. Although, the biimidazole moiety confers $[Ru(tmp)_2(bim)]^{2+}$ a higher dark toxicity, its encapsulation in hyaluronic acid–poly(lactic-*co*-glycolic acid) nanoparticles significantly reduced its dark toxicity while providing the selectivity necessary to target tumor cells. While we establish the phototoxicity of the photosensitizer and its nanoformulation, future studies will be focused on studying the efficacy of the compound under hypoxia and in clinically relevant tumor models. Structural modifications including functionalization of the two ancillary polypyridyl ligands with electron-withdrawing or electron-donating groups or the use of π-expanded tridentate ligands will be attempted to shift the absorption profile of the ruthenium-based dye towards the IR region to enhance its efficacy in deep seated tumors [77]. In summary, the Ru dye developed in this study shows high phototoxicity under blue light and can potentially be used on early oral cancers, photodisinfection procedures and management of viral infections including COVID-19 which is associated with hypoxia and hypoxemia [78]. Importantly, several previous studies have demonstrated the use of blue/green light for imaging and photodynamic therapy with different photosensitizers. Early studies with Photofrin have also suggested a distinct advantage of the use of green light (515 nm) in providing tumor control and limiting damage to healthy tissue in mesothelioma and bladder cancer models [79,80]. While the results reported in this study are encouraging, further investigations are however required to establish the photodynamic activity of the new Ru(II)-bim complexes on complex in vitro and in vivo models.

## CRediT authorship contribution statement

**José Quílez-Alburquerque:** Writing – review & editing, Writing – original draft, Visualization, Validation, Software, Methodology, Investigation, Formal analysis, Data curation, Conceptualization. **Mohammad Ahsan Saad:** Writing – original draft, Methodology, Investigation. **Ana B. Descalzo:** Writing – review & editing, Supervision, Resources, Project administration, Funding acquisition, Conceptualization. **Guillermo Orellana:** Writing – review & editing, Writing – original draft, Validation, Supervision, Resources, Project administration, Investigation, Conceptualization. **Tayyaba Hasan:** Writing – review & editing, Validation, Supervision, Resources, Project administration, Investigation, Funding acquisition, Conceptualization.

## Declaration of Competing Interest

The authors declare that they have no known competing financial interests or personal relationships that could have appeared to influence the work reported in this paper.

## Data availability

Data will be made available on request.

## Acknowledgment

This work was supported by grants from U.S. National Institutes of Health (NIH), UH2CA189901 and UH3CA189901, P01CA084203 and R01CA231606 to TH. This work was funded by the Spanish Ministry of Science and Innovation (grant RTI2018-096410-B-C22). J. Q.-A. thanks the Ministry for an F.P.I. doctoral grant. We thank Prof. S. Campuzano and Prof. M. Pedrero (Dpmt. of Analytical Chemistry, UCM) for their help with the electrochemical measurements in their equipment.

## Appendix A. Supplementary data

Supplementary data to this article can be found online at https://doi.org/10.1016/j.jphotochem.2022.114349.

## References

[1] R. Saini, N.V. Lee, K.Y.P. Liu, C.F. Poh, Prospects in the application of photodynamic therapy in oral cancer and premalignant lesions, Cancers 8 (2016) 83, https://doi.org/10.3390/cancers8090083.
[2] P. De Silva, M.A. Saad, H.C. Thomsen, S. Bano, S. Ashraf, T. Hasan, Photodynamic therapy, priming and optical imaging: Potential co-conspirators in treatment design and optimization, J. Porphyr. Phthalocyanines 24 (2020) 1320–1360, https://doi.org/10.1142/S1088424620300098.
[3] C.C. Tonon, S. Ashraf, J. Quilez-Alburquerque, A.N. de Souza Rastelli, T. Hasan, A. M. Lyons, A. Greer, Antimicrobial photodynamic inactivation using topical and superhydrophobic sensitizer techniques: A perspective from diffusion in biofilms, Photochem. Photobiol. (2021) 10.1111/php.13461.
[4] A. Wiehe, J.M. O'Brien, M.O. Senge, Trends and targets in antiviral phototherapy, Photochem. Photobiol. Sci. 18 (11) (2019) 2565–2612.
[5] S. Mallidi, K. Watanabe, D. Timerman, D. Schoenfeld, T. Hasan, Prediction of tumor recurrence and therapy monitoring using ultrasound-guided photoacoustic imaging, Theranostics 5 (2015) 289–301, https://doi.org/10.7150/thno.10155.

[6] M.S. Baptista, J. Cadet, A. Greer, A.H. Thomas, photosensitization Reactions of Biomolecules: Definition, Targets and mechanisms, Photochem. Photobiol. 97 (2021) 1456–1483, https://doi.org/10.1111/php.13470.

[7] M. Li, Y. Shao, J.H. Kim, Z. Pu, X. Zhao, H. Huang, T. Xiong, Y. Kang, G. Li, K. Shao, J. Fan, J.W. Foley, J.S. Kim, X. Peng, Unimolecular photodynamic $O_2$-economizer to overcome hypoxia resistance in phototherapeutics, J. Am. Chem. Soc. 142 (2020) 5380–5388, https://doi.org/10.1021/jacs.0c00734.

[8] M. Li, T. Xiong, J. Du, R. Tian, M. Xiao, L. Guo, S. Long, J. Fan, W. Sun, K. Shao, X. Song, J.W. Foley, X. Peng, Superoxide radical photogenerator with amplification effect: surmounting the achilles' heels of photodynamic oncotherapy, J. Am. Chem. Soc. 141 (2019) 2695–2702, https://doi.org/10.1021/jacs.8b13141.

[9] D. Chen, Q. Xu, W. Wang, J. Shao, W. Huang, X. Dong, Type I Photosensitizers Revitalizing Photodynamic Oncotherapy, Small 17 (2021) 2006742, https://doi.org/10.1002/smll.202006742.

[10] K. Zhang, Z. Yu, X. Meng, W. Zhao, Z. Shi, Z. Yang, H. Dong, X. Zhang, A bacteriochlorin-based metal-organic framework nanosheet superoxide radical generator for photoacoustic imaging-guided highly efficient photodynamic therapy, Adv. Sci. 6 (2019) 1–9, https://doi.org/10.1002/advs.201900530.

[11] L.K. McKenzie, H.E. Bryant, J.A. Weinstein, Transition metal complexes as photosensitisers in one- and two-photon photodynamic therapy, Coord. Chem. Rev. 379 (2019) 2–29, https://doi.org/10.1016/j.ccr.2018.03.020.

[12] S. Monro, K.L. Colón, H. Yin, J. Roque, P. Konda, S. Gujar, R.P. Thummel, L. Lilge, C.G. Cameron, S.A. McFarland, Transition metal complexes and photodynamic therapy from a tumor-centered approach: challenges, opportunities, and highlights from the development of TLD1433, Chem. Rev. 119 (2019) 797–828, https://doi.org/10.1021/acs.chemrev.8b00211.F.

[13] P.C. Lo, M.S. Rodríguez-Morgade, R.K. Pandey, D.K.P. Ng, T. Torres, F. Dumoulin, The unique features and promises of phtalocyanines as advanced photosensitizers for photodynamic therapy of cancer, Chem. Soc. Rev. 49 (2020) 1041–1056, https://doi.org/10.1039/c9cs00129h.

[14] F. Heinemann, J. Karges, G. Gasser, Critical overview of the use of Ru(II) polypyridyl complexes as photosensitizers in one-photon and two-photon photodynamic therapy, Acc. Chem. Res. 50 (2017) 2727–2736, https://doi.org/10.1021/acs.accounts.7b00180.

[15] F.E. Poynton, S.A. Bright, S. Blasco, D.C. Williams, J.M. Kelly, T. Gunnlaugsson, The development of ruthenium(II) polypyridyl complexes and conjugates for: In vitro cellular and in vivo applications, Chem. Soc. Rev. 46 (2017) 7706–7756, https://doi.org/10.1039/c7cs00680b.

[16] C.C. Tonon, S. Ashraf, A.N. de Souza Rastelli, G. Ghosh, T. Hasan, Q. Xu, A. Greer, A.M. Lyons, Evaluation of photosensitizer-containing superhydrophobic surfaces for the antibacterial treatment of periodontal biofilms, J. Photochem. Photobiol. B: Biol. (2022), 112458, https://doi.org/10.1016/j.jphotobiol.2022.112458.

[17] J.B. Shah, Correction of hypoxia, a critical element for wound bed preparation guidelines: $TIMEO_2$ principle of wound bed preparation, J Am Col Certif Wound Spec. 3 (2011) 26–32.

[18] E.B. Anderson, T.E. Long, Imidazole- and imidazolium-containing polymers for biology and material science applications, Polymer 51 (2010) 2447–2454, https://doi.org/10.1016/j.polymer.2010.02.006.

[19] P. Haegler, L. Joerin, S. Krähenbühl, J. Bouitbir, Hepatocellular toxicity of imidazole and triazole antimycotic agents, Toxicol. Sci. 157 (2017) 183–195, https://doi.org/10.1093/toxsci/kfx029.

[20] D. Sharma, B. Narasimhan, P. Kumar, V. Judge, R. Narang, E. De Clercq, J. Balzarini, Synthesis, antimicrobial and antiviral evaluation of substituted imidazole derivatives, Eur. J. Med. Chem. 44 (2009) 2347–2353, https://doi.org/10.1016/j.ejmech.2008.08.010.

[21] M.H. Hu, B.Y. Yu, X. Wang, G. Jin, Drug-like biimidazole derivatives dually target c-MYC/BCL-2 G-quadruplexes and inhibit acute myeloid leukemia, Bioorg. Chem. 104 (2020) 104264–104272, https://doi.org/10.1016/j.bioorg.2020.104264.

[22] A. Bergamo, G. Sava, Ruthenium anticancer compounds: Myths and realities of the emerging metal-based drugs, Dalton Trans. 40 (2011) 7817–7823, https://doi.org/10.1039/c0dt01816c.

[23] M. Mital, Z. Ziora, Biological applications of Ru(II) polypyridyl complexes, Coord. Chem. Rev. 375 (2018) 434–458, https://doi.org/10.1016/j.ccr.2018.02.013.

[24] Y. Liu, T. Chen, J. Liu, Y.S. Wong, Identification of fluorescent ruthenium complexes containing imidazole derivatives as a new class of apoptosis inducers by living cell real-time imaging, MedChemCom 4 (2013) 865–869, https://doi.org/10.1039/c3md20237b.

[25] S.A. Rommel, D. Sorsche, M. Fleischmann, S. Rau, Optical sensing of anions via supramolecular recognition with biimidazole complexes, Chem. Eur. J. 23 (2017) 18101–18119, https://doi.org/10.1002/chem.201605782.

[26] M.H. Chen, Y. Zheng, X.J. Cai, H. Zhang, F.X. Wang, C.P. Tan, W.H. Chen, L.N. Ji, Z.W. Mao, Inhibition of autophagic flux by cyclometalated Iridium(III) complexes through anion transportation, Chem. Sci. 10 (2019) 3315–3323, https://doi.org/10.1039/C8SC04520H.

[27] H.-J. Yu, Z.-F. Hao, H.-L. Peng, R.-H. Rao, M. Sun, A.W. Ross, C. Ran, H. Chao, L. Yu, Near-infrared lysosome pH tracker and naked-eye colorimetric nucleic acids sensor based on ruthenium complexes $[Ru(bim)_2(dppz)]^{2+}$ and $[Ru(bim)_2(pip)]^{2+}$, Sens. Actuators B: Chem. 252 (2017) 313–321, https://doi.org/10.1016/j.snb.2017.05.164.

[28] Y. Xia, Q. Chen, X. Qin, D. Sun, J. Zhang, J. Liu, Studies of Ruthenium(II)-2,2′-bisimidazole complexes on binding to G-quadruplex DNA and inducing apoptosis in HeLa cells, New J. Chem. 37 (2013) 3706–3715, https://doi.org/10.1039/c3nj00542a.

[29] M. Ouyang, L. Zeng, K. Qiu, Y. Chen, L. Ji, H. Chao, Cyclometalated $Ir^{III}$ Complexes as Mitochondria-Targeted Photodynamic Anticancer Agents, Eur. J. Inorg. Chem. 2017 (2017) 1764–1771, https://doi.org/10.1002/ejic.201601129.

[30] G. Orellana, M.L. Quiroga, C. De Dios, Spectroscopy, electrochemistry, and photochemistry of Ruthenium(II) complexes containing five-membered heterocyclic chelating ligands, Trends, Inorg. Chem. 3 (1993) 109–130.

[31] Z. Lv, H. Wei, Q. Li, X. Su, S. Liu, K.Y. Zhang, W. Lv, Q. Zhao, X. Li, W. Huang, Achieving efficient photodynamic therapy under both normoxia and hypoxia using cyclometalated Ru(II) photosensitizer through type I photochemical process, Chem. Sci. 9 (2018) 502–512, https://doi.org/10.1039/c7sc03765a.

[32] Y.Y. Wang, Y.C. Liu, H. Sun, D.S. Guo, Type I photodynamic therapy by organic–inorganic hybrid materials: From strategies to applications, Coord. Chem. Rev. 395 (2019) 46–62, https://doi.org/10.1016/j.ccr.2019.05.016.

[33] J. Du, T. Shi, S. Long, P. Chen, W. Sun, J. Fan, X. Peng, Enhanced photodynamic therapy for overcoming tumor hypoxia: From microenvironment regulation to photosensitizer innovation, Coord. Chem. Rev. 427 (2021) 213604–213621, https://doi.org/10.1016/j.ccr.2020.213604.

[34] S.S. Lucky, K.C. Soo, Y. Zhang, Nanoparticles in photodynamic therapy, Chem. Rev. 115 (2015) 1990–2042, https://doi.org/10.1021/cr5004198.

[35] G. Tripodo, A. Trapani, M.L. Torre, G. Giammona, G. Trapani, D. Mandracchia, Hyaluronic acid and its derivatives in drug delivery and imaging: Recent advances and challenges, Eur. J. Pharm. Biopharm. 97 (2015) 400–416, https://doi.org/10.1016/j.ejpb.2015.03.032.

[36] G. Huang, H. Huang, Application of hyaluronic acid as carriers in drug delivery, Drug Deliv. 25 (2018) 766–772, https://doi.org/10.1080/10717544.2018.1450910.

[37] M.N. Collins, C. Birkinshaw, Hyaluronic acid based scaffolds for tissue engineering – a review, Carbohydr. Polym. 92 (2013) 1262–1279, https://doi.org/10.1016/j.carbpol.2012.10.028.

[38] S. Misra, V.C. Hascall, R.R. Markwald, S. Ghatak, Interactions between hyaluronan and its receptors (CD44, RHAMM) regulate the activities of inflammation and cancer, Front. Immunol. 6 (2015) 1–31, https://doi.org/10.3389/fimmu.2015.00201.

[39] G. Huang, H. Huang, Hyaluronic acid-based biopharmaceutical delivery and tumor-targeted drug delivery system, J. Control. Release 278 (2018) 122–126, https://doi.org/10.1016/j.jconrel.2018.04.015.

[40] F. Dosio, S. Arpicco, B. Stella, E. Fattal, Hyaluronic acid for anticancer drug and nucleic acid delivery, Adv. Drug Deliv. Rev. 97 (2016) 204–236, https://doi.org/10.1016/j.addr.2015.11.011.

[41] K.Y. Choi, K.H. Min, J.H. Na, K. Choi, K. Kim, J.H. Park, I.C. Kwon, S.Y. Jeong, Self-assembled hyaluronic acid nanoparticles as a potential drug carrier for cancer therapy: Synthesis, characterization, and in vivo biodistribution, J. Mater. Chem. 19 (2009) 4102–4107, https://doi.org/10.1039/b900456d.

[42] A. Saneja, D. Arora, R. Kumar, R.D. Dubey, A.K. Panda, P.N. Gupta, CD44 targeted PLGA nanomedicines for cancer chemotherapy, Eur. J. Pharm. Sci. 121 (2018) 47–58, https://doi.org/10.1016/j.ejps.2018.05.012.

[43] K.Y. Choi, H.Y. Yoon, J.H. Kim, S.M. Bae, R.W. Park, Y.M. Kang, I.S. Kim, I. C. Kwon, K. Choi, S.Y. Jeong, K. Kim, J.H. Park, Smart nanocarrier based on PEGylated hyaluronic acid for cancer therapy, ACS Nano 5 (2011) 8591–8599, https://doi.org/10.1021/nn202070n.

[44] W. Li, C. Zheng, Z. Pan, C. Chen, D. Hu, G. Gao, S. Kang, H. Cui, P. Gong, L. Cai, Smart hyaluronidase-actived theranostic micelles for dual-modal imaging guided photodynamic therapy, Biomaterials 101 (2016) 10–19, https://doi.org/10.1016/j.biomaterials.2016.05.019.

[45] S. Gao, J. Wang, R. Tian, G. Wang, L. Zhang, Y. Li, L. Li, Q. Ma, L. Zhu, Construction and evaluation of a targeted hyaluronic acid nanoparticle/photosensitizer complex for cancer photodynamic therapy, ACS Appl. Mater. Interfaces 9 (2017) 32509–32519, https://doi.org/10.1021/acsami.7b09331.

[46] B.A. Buhren, H. Schrumpf, N.P. Hoff, E. Bölke, S. Hilton, P.A. Gerber, Hyaluronidase: From clinical applications to molecular and cellular mechanisms, Eur. J. Med. Res. 21 (2016) 1–7, https://doi.org/10.1186/s40001-016-0201-5.

[47] E. Villemin, Y.C. Ong, C.M. Thomas, G. Gasser, Polymer encapsulation of ruthenium complexes for biological and medicinal applications, Nat. Rev. Chem. 3 (2019) 261–282, https://doi.org/10.1038/s41570-019-0088-0.

[48] E.C. Johnson, B.P. Sullivan, D.J. Salmon, S.A. Adeyemi, T.J. Meyer, Synthesis and properties of the chloro-bridged dimer $[(bpy)_2RuCl]_2^{2+}$ and its transient 3+ mixed-valence ion, Inorg. Chem. 17 (1978) 2211–2215, https://doi.org/10.1021/ic50186a038.

[49] R. Schmidta, C. Tanielian, R. Dunsbach, C. Womb, Phenalenone, a universal reference compound for the determination of quantum yields of singlet oxygen $O_2$ ($^1\Delta_g$) sensitization, J. Photochem. Photobiol. A: Chem. 79 (1994) 11–17.

[50] D. García-Fresnadillo, Y. Georgiadou, G. Orellana, A.M. Braun, E. Oliveros, Singlet-oxygen ($^1\Delta_g$) production by ruthenium(II) complexes containing polyazaheterocyclic ligands in methanol and in water, Helv. Chim. Acta 79 (1996) 1222–1238, https://doi.org/10.1002/hlca.19960790428.

[51] K. Debowska, D. Debski, M. Hardy, M. Jakubowska, B. Kalyanaraman, A. Marcinek, R. Michalski, B. Michalowski, O. Ouari, A. Sikora, R. Smulik, J. Zielonka, Toward selective detection of reactive oxygen and nitrogen species with the use of fluorogenic probes – Limitations, progress, and perspectives, Pharmacol. Reports 67 (2015) 756–764, https://doi.org/10.1016/j.pharep.2015.03.016.

[52] J. Huang, H. Zhang, Y. Yu, Y. Chen, D. Wang, G. Zhang, G. Zhou, J. Liu, Z. Sun, D. Sun, Y. Lu, Y. Zhong, Biodegradable self-assembled nanoparticles of poly(D, L-lactide-co-glycolide)/hyaluronic acid block copolymers for target delivery of docetaxel to breast cancer, Biomaterials 35 (2014) 550–566, https://doi.org/10.1016/j.biomaterials.2013.09.089.

[53] M.A. Saad, M. Xavierselvan, H.A. Sharif, S. Selfridge, R. Pawle, M. Varvares, S. Mallidi, T. Hasan, Dual function antibody conjugates for multimodal imaging and photoimmunotherapy of cancer cells, Photochem. Photobiol.. 98 (2022) 220–231, https://doi.org/10.1111/php.13501.

[54] M.A. Saad, L. Contreras, S. Bano, S. Selfridge, Z. Mai, R. Pawle, M. Varvares, S. Mallidi, T. Hasan, EGFR-targeted multi-modal molecular imaging and treatment in a heterocellular model of head and neck cancer, Proc. SPIE (2022), https://doi.org/10.1117/12.2610047.
[55] C.A. Puckett, J.K. Barton, Methods to explore cellular uptake of ruthenium complexes, J. Am. Chem. Soc. 129 (2007) 46–47, https://doi.org/10.1021/ja0677564.
[56] H. Komatsu, K. Yoshihara, H. Yamada, Y. Kimura, A. Son, S.I. Nishimoto, K. Tanabe, Ruthenium complexes with hydrophobic ligands that are key factors for the optical imaging of physiological hypoxia, Chem. Eur. J. 19 (2013) 1971–1977, https://doi.org/10.1002/chem.201202809.
[57] S. Nonell, C. Flors, in: S. Nonell, C. Flors (Eds.), Steady-State and Time-Resolved Singlet Oxygen Phosphorescence Detection in the Near-IR, The Royal Society of Chemistry, Cambridge, UK, 2016, pp 7–26. 10.1039/9781782622130-FP007.
[58] J. Chen, S.C. Rogers, M. Kavdia, Analysis of kinetics of dihydroethidium fluorescence with superoxide using xanthine oxidase and hypoxanthine assay, Ann. Biomed. Eng. 41 (2013) 327–337, https://doi.org/10.1007/s10439-012-0653-x.
[59] R. Michalski, B. Michalowski, A. Sikora, J. Zielonka, B. Kalyanaraman, On the use of fluorescence lifetime imaging and dihydroethidium to detect superoxide in intact animals and ex vivo tissues: A reassessment, Free Radic. Biol. Med. 67 (2014) 278–284, https://doi.org/10.1016/j.freeradbiomed.2013.10.816.
[60] J.L. Clément, N. Ferré, D. Siri, H. Karoui, A. Rockenbauer, P. Tordo, Assignment of the EPR spectrum of 5,5-dimethyl-1-pyrroline N-oxide (DMPO) superoxide spin adduct, J. Org. Chem. 70 (2005) 1198–1203, https://doi.org/10.1021/jo048518z.
[61] M.A. Saad, M.R. Ch, Condition responsive nanoparticles for managing infection and inflammation in keratitis, Nanoscale 9 (2017) 9946–9959, https://doi.org/10.1039/C7NR00922D.
[62] Y. Cu, M. Saltzman, Controlled surface modification with poly(ethylene)glycol enhances diffusion of PLGA nanoparticles in human cervical mucus, Mol. Pharm. 6 (2009) 173–181, https://doi.org/10.1021/mp8001254.
[63] S. Uthaman, A.P. Mathew, H.J. Park, B. Il Lee, H.S. Kim, K.M. Huh, I.K. Park, IR 780-loaded hyaluronic acid micelles for enhanced tumor-targeted photothermal therapy, Carbohydr. Polym. 181 (2018) 1–9.
[64] K. Mitra, M. Samsó, C.E. Lyons, M.C.T. Hartman, Hyaluronic acid grafted nanoparticles of a platinum(II)-silicon(IV) phthalocyanine conjugate for tumor and mitochondria-targeted photodynamic therapy in red light, J. Mater. Chem. B 6 (2018) 7373–7377, https://doi.org/10.1039/C8TB02533A.
[65] I.S. Bayer, Hyaluronic acid and controlled release: a review, Molecules 25 (2020) 2649–2687, https://doi.org/10.3390/molecules25112649.
[66] V. Pierroz, T. Joshi, A. Leonidova, C. Mari, J. Schur, I. Ott, L. Spiccia, S. Ferrari, G. Gasser, Molecular and cellular characterization of the biological effects of ruthenium(II) complexes incorporating 2-pyridyl-2-pyrimidine-4-carboxylic acid, J. Am. Chem. Soc. 134 (2012) 20376–20387, https://doi.org/10.1021/ja307288s.
[67] X. Wang, S. Peralta, C.T. Moraes, in: Kenneth D. Tew, Paul B. Fisher (Eds.), Mitochondrial alterations during carcinogenesis: A review of metabolic transformation and targets for anticancer treatments, Academic Press, 2013. pp. 127–160. 10.1016/B978-0-12-407190-2.00004-6.
[68] J. Xu, F. Zeng, H. Wu, C. Hu, S. Wu, Enhanced photodynamic efficiency achieved via a dual-targeted strategy based on photosensitizer/micelle structure, Biomacromolecules 15 (2014) 4249–4259, https://doi.org/10.1021/bm501270e.
[69] S.M. Mahalingam, J.D. Ordaz, P.S. Low, Targeting of a photosensitizer to the mitochondrion enhances the potency of photodynamic therapy, ACS Omega 3 (2018) 6066–6074, https://doi.org/10.1021/acsomega.8b00692.
[70] E. Buytaert, M. Dewaele, P. Agostinis, Molecular effectors of multiple cell death pathways initiated by photodynamic therapy, Biochim. Biophys. Acta-Rev Cancer 1776 (2007) 86–107, https://doi.org/10.1016/j.bbcan.2007.07.001.
[71] V. Inguscio, E. Panzarini, L. Dini, Autophagy contributes to the death/survival balance in cancer photodynamic therapy cells, Cells 1 (2012) 464–491, https://doi.org/10.3390/cells1030464.
[72] D. Kessel, Y. Luo, Photodynamic therapy: A mitochondrial inducer of apoptosis, Cell Death Differ. 6 (1999) 28–35, https://doi.org/10.1038/sj.cdd.4400446.
[73] D. Kessel, N.L. Oleinick, Cell death pathways associated with photodynamic therapy: An update, Photochem. Photobiol. 94 (2018) 213–218, https://doi.org/10.1111/php.12857.
[74] S. Estalayo-Adrián, S. Blasco, S.A. Bright, G.J. McManus, G. Orellana, D. C. Williams, J.M. Kelly, T. Gunnlaugsson, Water-soluble amphiphilic ruthenium(II) polypyridyl complexes as potential light-activated therapeutic agents, Chem. Comm. 56 (2020) 9332–9335, https://doi.org/10.1039/d0cc04397d.
[75] J. Karges, F. Heinemann, M. Jakubaszek, F. Maschietto, C. Subecz, M. Dotou, R. Vinck, O. Blacque, M. Tharaud, B. Goud, E. Viñuelas Zahínos, B. Spingler, I. Ciofini, G. Gasser, Rationally designed long-wavelength absorbing Ru(II) polypyridyl complexes as photosensitizers for photodynamic therapy, J. Am. Chem. Soc. 142 (2020) 6578–6587, https://doi.org/10.1021/jacs.9b13620.
[76] J. Karges, F. Heinemann, F. Maschietto, M. Patra, O. Blacque, I. Ciofini, B. Spingler, G. Gasser, A Ru(II) polypyridyl complex bearing aldehyde functions as a versatile synthetic precursor for long-wavelength absorbing photodynamic therapy photosensitizers, Bioorganic, Med. Chem. 27 (2019) 2666–2675, https://doi.org/10.1016/j.bmc.2019.05.011.
[77] L.M. Lifshits, J.A. Roque, E. Ramasamy, R.P. Thummel, C.G. Cameron, S. A. McFarland, Ruthenium photosensitizers for NIR PDT require lowest-lying triplet intraligand ($^3$IL) excited states, J. Photochem. Photobiol. 8 (2021), 100067, https://doi.org/10.1016/j.jpap.2021.100067.
[78] J. Herrmann, V. Mori, J.H.T. Bates, B. Suki, Modeling lung perfusion abnormalities to explain early COVID-19 hypoxemia, Nat. Commun. 11 (2020) 4883, https://doi.org/10.1038/s41467-020-18672-6.
[79] T.H. Foster, S.L. Gibson, R.F. Raubertas, Response of photofrin-sensitized mesothelioma xenografts to photodynamic therapy with 514 nm light, Br. J. Cancer 73 (1996) 933–936, https://doi.org/10.1038/bjc.1996.184.
[80] U.O. Nseyo, R.K. Whalen, S.L. Lundahl, Canine bladder response to red and green light whole bladder photodynamic therapy, Invest. Urol. 41 (1993) 392–396, https://doi.org/10.1016/0090-4295(93)90607-c.